Heliyon 8 (2022) e10442

Contents lists available at ScienceDirect

Heliyon

journal homepage: www.cell.com/heliyon

Research article

Study on the mechanism of the black crust formation on the ancient marble sculptures and the effect of pollution in Beijing area

Feng Wang [a,**], Yingchun Fu [a], Di Li [b], Yazhen Huang [a], Shuya Wei [a,*]

[a] Institute for Cultural Heritage and History of Science & Technology, University of Science and Technology Beijing, China
[b] Beijing Stone Carving Art Museum, China

ARTICLE INFO

Keywords:
Black crusts
Gypsum
Pollution sources
Meteorology
Forming mechanism
Marble

ABSTRACT

In Beijing area, the precious stone objects often suffer from the black crusts on the specific parts of the objects, in order to understand the forming mechanism of the black crusts, samples from the stone sculptures in Beijing Stone Carving Art Museum, ZHIHUA Temple and Museum of Western Zhou Yandu Relics were taken and studied. Nondestructive measurement was carried out firstly to acquire main elements of the samples by portable X-ray spectrum (pXRF). Morphology and microstructure of typical black crust samples were examined by ultra-depth of field microscope (UDFM) and scanning electron microscopy coupled with energy dispersive spectroscopy (SEM-EDS). Compositions of black crusts and body rocks were evaluated with X-ray diffraction (XRD), Raman spectra and mapping. Inductively coupled plasma optical emission spectrometry (ICP-OES) and pyrolysis-gas chromatography/mass spectrometry (Py-GCMS) were used to identify the major pollution sources leading to the black crusts.

Through this study, the composition of the black crusts was revealed. Different gypsum crystals and carbonaceous species were found. Pollutant elements analysis and pyrolysis products provide indicators of the pollution sources. As consequence of strong photochemical oxidation processes and the high temperature from June to September in Beijing, more acid rain precursors can be formed. Frequent sulphation process occurs on the $CaCO_3$/$CaMg(CO_3)_2$ surface. Combining morphology results and atmospheric data, the formation of black crusts in Beijing can be deduced.

1. Introduction

Beijing originates from Jin State more than 3000 years ago and became a national political center from Liao dynasty (AD 916–1125) (http://english.beijing.gov.cn/). In the process of urban construction, the sculptures and constructions were usually made of marble, owing to the abundant mineral resources in Dashiwo Town, Fangshan district, Beijing (Tuotuo, 1995 Yuan Dynasty; Xiao, 1983, Ming Dynasty). The Beijing marble includes a famous jade-like white rock, named Hanbaiyu marble (HM), and a kind of greenish white marble called Qingbaishi marble (QM). The petrologic feature of Beijing marble was studied by Liu J-b and Zhang Z.J (Liu et al., 2019). The main mineral is dolomite ($CaMg(CO_3)_2$) and porosity is very low (1–2%) (Liu et al., 2019). In recent decades, more black crusts were found on these ancient marble sculptures (Zhang et al., 2016) due to the rapid urban and industrial development in Beijing.

The formation of black crusts on limestone and marble surface is a well-known deterioration process on account of air pollutants, successively the authors can introduce the specific case study. Sulphation between the carbonate and sulfur compounds occurs and induces the transformation of the carbonate, such as calcite ($CaCO_3$) and dolomite ($CaMg(CO_3)_2$), into gypsum ($CaSO_4{\cdot}2H_2O$). Polyporous gypsum can adsorb elemental carbon and other carbonaceous particles, result in a black color (Camuffo et al., 1983; Galletti et al., 1997; Barca et al., 2014; Russa et al., 2013). The atmospheric metal pollution is recognized as efficient catalysts for the oxidation of SO_2, leading to more calcium sulfate sediment (Camuffo et al., 1983). The rate of crusts formation depends on the concentration of sulphur-containing pollutants and property of subjacent stones (Sabbioni, 1995; Bugini et al., 2000; Marinoni et al., 2003; Fronteau et al., 2010).

Researchers tried to understand the whole process better through studying black crusts from different places, such as the Seville Cathedral

* Corresponding author.
** Corresponding author.
E-mail addresses: wangfeng1911@126.com (F. Wang), swei@ustb.edu.cn (S. Wei).

https://doi.org/10.1016/j.heliyon.2022.e10442
Received 23 May 2022; Received in revised form 1 August 2022; Accepted 22 August 2022

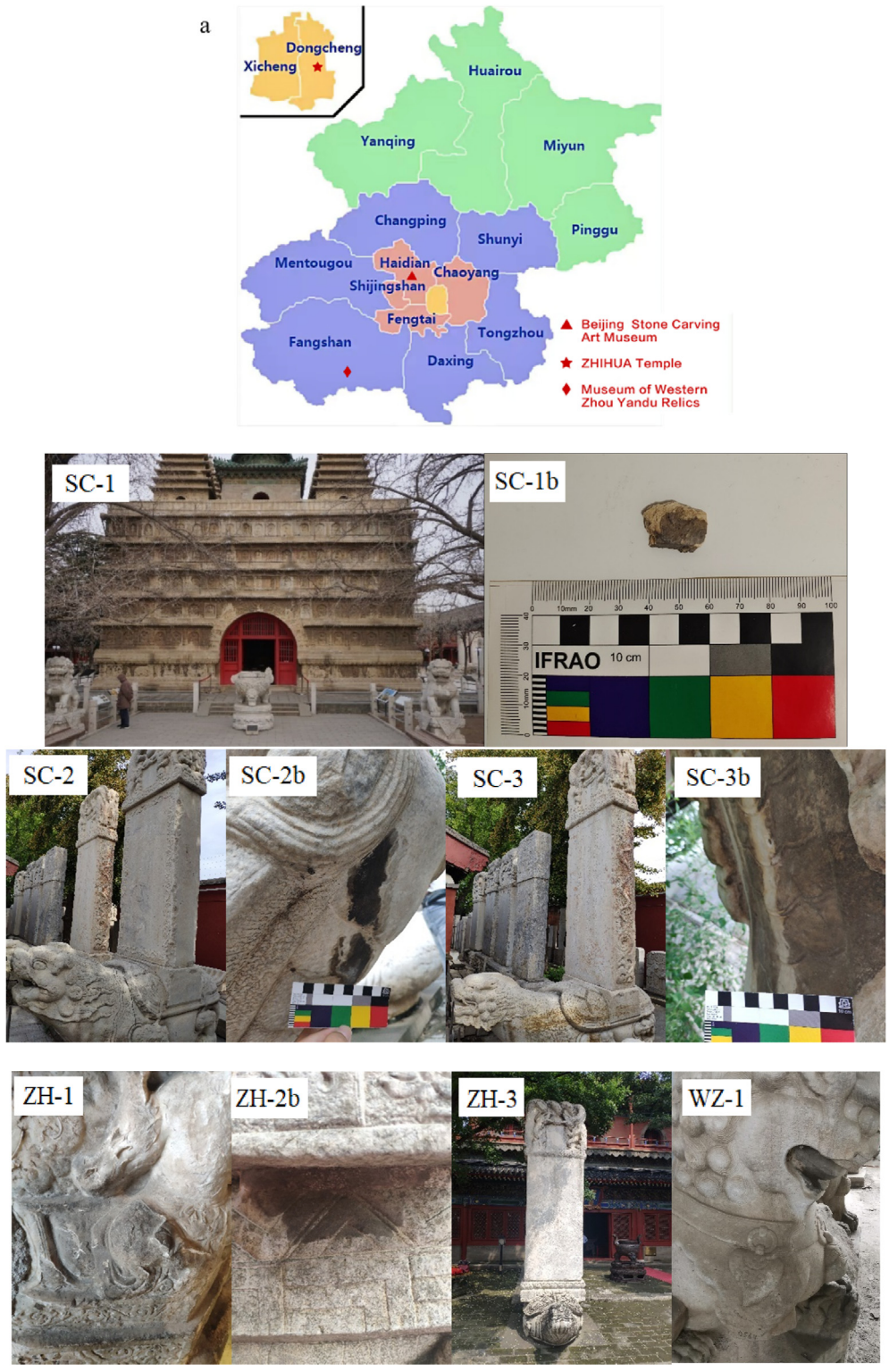

Figure 1. Sampled three sites in Beijing area (a) and Typical Sampling locations.

(Ruffolo et al., 2015), the Oceanus statue of the Fontana di Trevi (Rome) (La Russa et al., 2017), Halberstadt church (Germany) (Farkas et al., 2018), the Triumphal Arch of Galerius in Thessaloniki, Greece (Samara et al., 2020), the cathedral of Monza (Comite et al., 2020), the Punta Begona Galleries (Garcí a-Florentino et al., 2020), and so on. Meanwhile, different methods including spectrometric analysis (Nord and Ericsson, 1993; Potgieter-Vermaak et al., 2005; B Belfiore et al., 2013; Lamhasni et al., 2019), microscopic characterization (Pozo-Antonio et al., 2017), Chemical-Thermal quantitative methodology (Bonazza et al., 2005; Nadia et al., 2006), trace elements examination (Russa et al., 2013; Samara et al., 2020), sulphur and oxygen isotope analysis (Rivas et al., 2014; Genot et al., 2020; Aroskay et al., 2021) were used to figure out microstructure, chemical features and pollution sources of the black crusts.

In Beijing area, the crusts are mainly found on specific parts of the Chinese characteristic sculptures, for instance on the neck of BiXi (Stone

Table 1. Samples and their description (WM: White calcitic marble), Sample number + a = host rock, Sample number + b = black crust.

Sample number	Name of culture relics	Locality	Host rock
SC-1	Vajrasana Pagoda	Falling debris at the East part of Pagoda	WM
SC-2	Deming monument	Neck of Stone Turtle	QM
SC-3	Imperial Titling Stele for Haise	Neck of Stone Turtle	WM
SC-4	Stele of Guandi temple rebuilding	Emblazonment of stele	QM
SC-5	Stele of Fu Heng's Ancesiral Temple	Neck of Stone Turtle	QM
SC-6	Stele of Conferring the Posthumous Title on Yang Tingzhang	Neck of Stone Turtle	QM
SC-7	Imperial Titling Stele for Wu Nuchun	Neck of Stone Turtle	QM
SC-8	Imperial Titling Stele for Fu Kuanchan	Tongue of Stone Turtle	QM
SC-9	Stele of Chu area learning school	Neck of Stone Turtle	QM
SC-10	Stele of Xianying aoist temple rebuilding	Emblazonment of stele	QM
SC-11	Stele of Xingsheng Nunnery founding	Emblazonment of stele	QM
SC-12	Stele of original inscriptional records	Emblazonment of stele	QM
ZH-1	Mandala in the Pavilion of Sutta Pitaka	North side of Mandala	WM
ZH-2	East stele in front of the tathagata Pavilion	Junction of Stone Turtle and stele	QM
ZH-3	West stele in front of the tathagata Pavilion	Neck of Stone Turtle	QM
WZ-1	Stone Lion No.0564	Tongue of Stone Lion	QM

Turtle) and in the mouth of stone lions. In this work, we present the study result of the black crusts from several cultural relic sites to reveal the mechanism of the formation of black crust on the stone sculpture in Beijing, to discuss the effect of the pollution and local climate to the black crust.

2. Materials and methods

2.1. Sample description

Black crust samples were taken from 3 sites, Beijing Stone Carving Art Museum (SC) located in Haidian district, ZHIHUA Temple (ZH) located in Dongcheng district and Museum of Western Zhou Yandu Relics (WZ) located in Fangshan district, as shown in Figure 1a. The sketch map of Beijing was downloaded from China Discovery website (https://www.chinadiscovery.com/beijing-tours/maps/). Urbanization could affect the air pollution emission patterns and meteorological conditions (Bao et al., 2019; Chen et al., 2021a,b). Two sites are close to the center of city, which have high urbanization level, while the one in Fangshan district is far from the city center, surrounded by villages.

Twelve samples were taken from the objects in Beijing Stone Carving Art Museum (SC) (Samples a are host rocks and Samples b are black crusts), where Vajrasana Pagoda has been standing in the monastery since over 500 years ago (http://www.bjstoneartmuseum.org.cn/Museum/).

Three samples were taken from Mandala in the Pavilion of Sutta Pitaka, Stone Turtle in front of the tathagata Pavilion in ZHIHUA Temple (ZH), seen in Figure 1-ZH1-3 and Table 1, which was built in 1444 AD (http://www.zhihuatemple.com/Temple/Introducation/).

One sample was taken from the Tongue of the Stone Lion in the storehouse at the east of the main hall, in Museum of Western Zhou Yandu Relics (WZ) (see the detail information of the samples in Figure 1-WZ and Table 1) (http://wwj.beijing.gov.cn/bjww/362771/362772/545823/index.html).

2.2. Data resource

The climate of Beijing is a typical semi-humid continental monsoon climate. It is hot and rainy in summer, cold and dry in winter, spring and autumn are relatively short (Pak et al., 2020). In this study, air quality data, ambient temperature and relative humidity of 81 months from January 2014 to August 2020 were acquired from the Ministry of Ecology and Environment of the People's Republic of China (http://www.mee.gov.cn/) and a public software platform (https://www.aqistudy.cn/). To ensure the accuracy of these data, we used the average data per month which deleted the abnormal one.

2.3. Methods of characterization

Samples were analyzed for a suite of elements on site by X-ray spectrum using a Thermo Scientific Niton XL3t 950 portable XRF device (pXRF), which was equipped with a 50 kV x-ray tube (max. 50 kV, 200 μA) with an Ag anode target excitation source. The 3mm diameter beam spot and mining Cu/Zn mode were used for measuring small black crusts.

Surface morphology and microstructure was studied by ultra-depth of field microscope (UDFM) and scanning electron microscopy coupled with energy dispersive spectroscopy (SEM-EDS). Microscope images were recorded using a Leica DVM6 and processed by LAS X software. SEM results were obtained through the TESCAN VEGA3 electron microscope (TESCAN ANALYTICS), operated at an accelerating voltage of 20 kV, coupled with a Bruker Xflash 6160 EDS detector.

Raman spectra and mapping results were measured with a HORIBA Scientific XploRA PLUS spectrometer at room temperature, using 785nm laser excitation, Olympus 50X LWD visible objective. The laser power on the samples was about 1 mW, while slit and hole were set as 100 and 300, respectively. Spectra processing was performed using LabSpec software version 6.4.4. Mapping results were acquired without any adhesive on the glass slide, with 1.5 μm steps and 3 s acquisition time per spectrum. Raman image was obtained through Classical Least Squares (CLS) calibration.

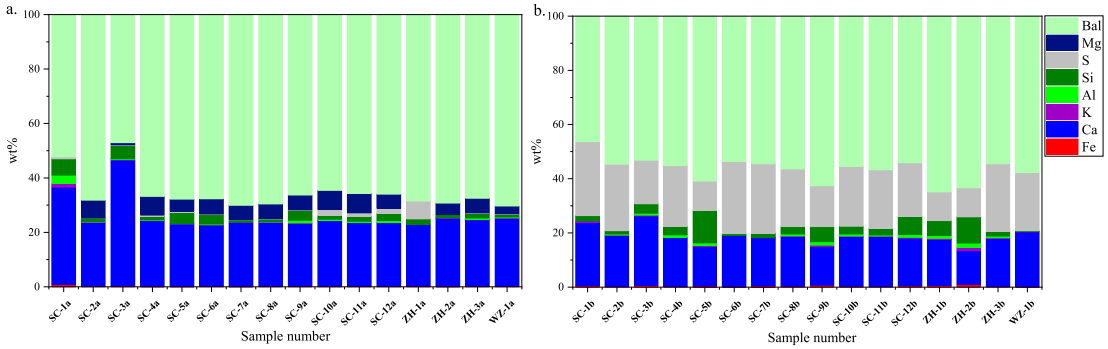

Figure 2. Main elements data based on pXRF of the host rock(a) and black crusts(b), unit: wt%, Bal = Balance signal stands for the amount of unmeasured residues.

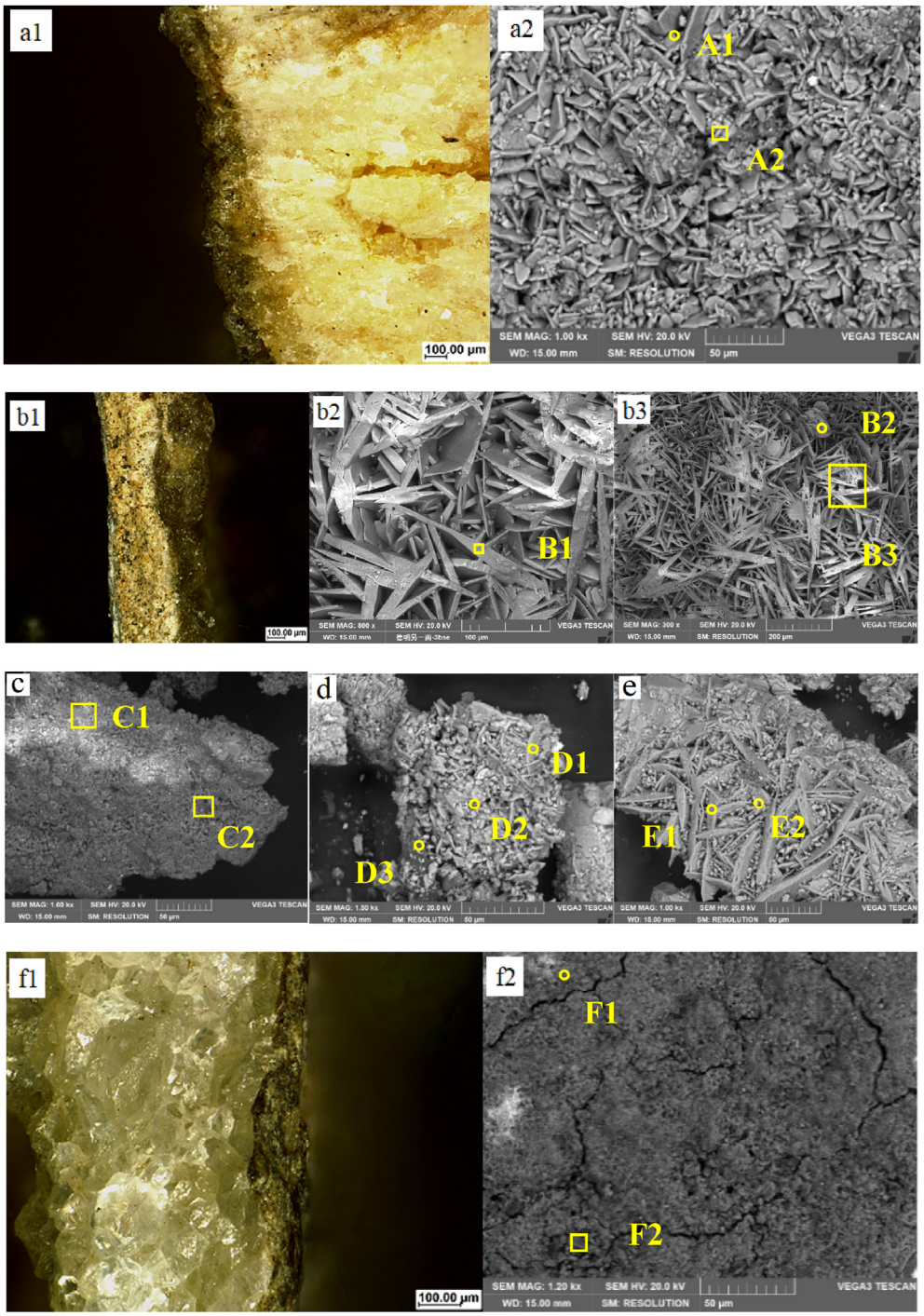

Figure 3. UDFM and SEM images of samples. a:SC-1b; b:SC-2b; c: ZH-1b; d: ZH-2b; e: ZH-3b; f: WZ-1b, EDS data was acquired from the capital letter positions.

For X-ray diffraction (XRD) analysis, the measurement was operated with Rigaku Smartlab at 40 Kv, 30 mA and CuKα radiation, range of 10–90° 2θ and 0.02º 2θ step size. After collecting the data, the Rietveld method was used to quantify the phase compositions of the stones.

Quantitative metal content of the black crusts was determined by inductively coupled plasma optical emission spectrometry (ICP-OES) performed on an Agilent 730 spectrometer. Samples were analyzed using the following acquisition parameters: 1.0Kw RF power, Argon gas, 15L/min plasma flow, 1.5L/min auxiliary gas flow, 0.75L/min nebulizer gas flow, Axial detector Mode, Linear calibration type.

The pyrolysis gas chromatography mass spectrometry (Py-GCMS) analysis was accomplished with Frontier Lab PY-3030D pyrolyzer, attached to Shimadzu QP2010Ultra GCMS spectrometry. About 0.2 mg dry samples were introduced into the pyrolyzer by the autosampler in a sample cup. Pyrolysis was performed at 550 °C for 20 s, and the interface and GC injector were set at 290 °C with split injection mode. Agilent DB-5MS UI (5% diphenyl/95% dimethyl siloxane) capillary column (0.18 mm internal diameter, 20 m length, 0.18 m film thickness) was used. Initial temperature of the column oven was 35 °C, and then heated to 315 °C in three processes (35–100 °C, 60 °C/min; 100–250 °C, 14 °C/min; 250–315 °C, 6 °C/min, holding at 315 °C for 1.5 min). The Helium carrier gas with a 145.3 kPa inlet pressure and 1:20 split ratio was set to the linear velocity mode. Scanning range of the MS was 35–500 m/z at 70 eV, while the interface was held at 250 °C and the ion source was kept at 200

Table 2. EDS data of scraped samples (Unit: wt%, n.d. = not determined).

Sample No.	Position	C	O	Na	Mg	Al	Si	S	Cl	K	Ca	Fe	Cu
SC-1b	A1	2.92	50.42	0.32	0.06	0.58	1.18	15.24	n.d.	0.26	28.84	0.18	n.d.
SC-1b	A2	7.91	45.26	0.51	0.54	2.83	6.21	21.04	n.d.	1.00	12.83	1.87	n.d.
SC-2b	B1	5.75	59.61	n.d.	0.09	0.13	0.30	13.39	n.d.	n.d.	20.74	n.d.	n.d.
SC-2b	B2	7.52	60.28	n.d.	n.d.	n.d.	0.19	12.79	n.d.	n.d.	19.23	n.d.	n.d.
SC-2b	B3	6.58	60.69	n.d.	n.d.	0.63	0.63	13.73	n.d.	n.d.	18.37	n.d.	n.d.
ZH-1b	C1	9.66	54.8	n.d.	0.47	0.83	2.75	13.26	0.91	0.79	13.52	3.00	n.d.
ZH-1b	C2	9.45	51.01	n.d.	n.d.	0.94	3.43	13.13	0.77	0.83	16.81	2.98	0.64
ZH-2b	D1	6.06	58.12	n.d.	0.42	0.55	1.01	11.52	n.d.	0.30	20.66	0.75	0.61
ZH-2b	D2	11.6	48.53	0.34	1.56	3.85	15.42	0.31	0.39	1.87	11.53	3.94	0.66
ZH-2b	D3	24.39	47.71	0.56	3.07	0.99	3.86	5.41	1.78	1.21	10.15	0.86	n.d.
ZH-3b	E1	5.13	56.27	n.d.	0.14	n.d.	0.16	15.3	n.d.	n.d.	22.99	n.d.	n.d.
ZH-3b	E2	3.51	61.97	n.d.	0.19	n.d.	0.11	14.52	n.d.	n.d.	19.57	0.14	n.d.
WZ-1b	F1	9.16	49.24	0.38	1.05	3.04	6.44	0.70	n.d.	1.02	21.05	2.44	n.d.
WZ-1b	F2	8.30	53.55	0.84	1.15	11.81	13.51	0.49	n.d.	1.80	3.46	5.09	n.d.

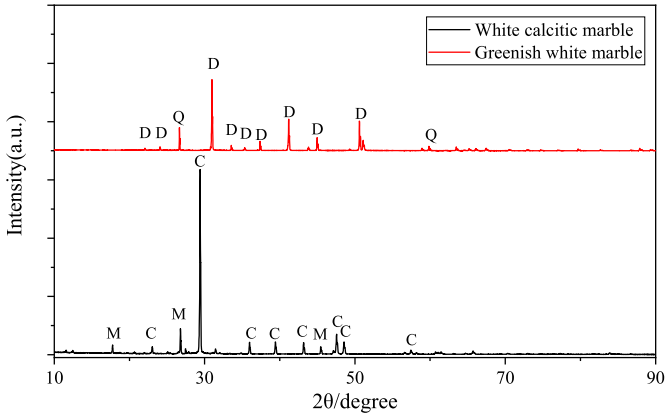

Figure 4. XRD patterns of the white calcitic marble (SC-1a) and QM(ZH-3a), C(CaCO3:PDF-85-1108), M(Muscovite, PDF:46–1409), D(Dolomite, PDF:75–1762), Q(Quartz, PDF:85–0795).

°C. The compounds were identified through AMDIS program developed by the National Institute of Standards and Technology (NIST).

3. Results

3.1. Nondestructive testing by pXRF

Nondestructive measurement was firstly carried out to characterize main elements by pXRF. Overall, about 24 sculptures have evident gypsum-rich black crusts in the three sites. The chemical element contents of host rock and crusts are shown in Figure 2, without normalization. As displayed in Figure 2a, most body rocks are QM, rooting in its color. Concentrations of Ca in these QMs are between 22wt% and 27wt%, while Mg are between 2 wt% to 7 wt% and Fe, Al and K are common but with low amount, being similar with Wang Z's results (Wang et al., 2022). Two substrates (SC-1a, SC-3a) have higher concentrations of calcium, which are more than 35wt% and concentrations of magnesium are below limit of detection, described as white calcitic marble (WM). As can be seen in Figure 2b, sulphur content of the black crusts is obviously higher, ranging from 10wt% to 30 wt%. All samples exhibit Si content varying from 1% to 6.6%, except SC-5b and ZH-2b. Si content in samples of SC-5b and ZH-2b is around 10%.

3.2. Microscope and SEM-EDS

In order to preserve the original form, the samples were not polished or Au/carbon sputtered. Figure 3 and Figure 3s. shows the surface morphology and microstructure of the scraped samples and Table 2 reveals the elements contents of crystals and particles. The good conductivity of samples indicates abundant carbon on the surface in an air less chamber (7.5×10^{-2} Pa).

The thickness of black crusts on SC-1b ranges from 100 to 273μm, seen in Figure 3a. Idiomorphic gypsum crystals were rhombic and laminar in 17–60μm length, darker than transparent particles. EDS data suggests the crystals are composed of calcium sulphate and carbonaceous matters, particles may contain more soil sediments and black carbon according to more C, Al, Si, K and Fe.

SC-2b has a special layered structure from inside to outside, displayed in Figure 3b. The innermost black layer (right part) varies from 180 to 291μm, containing acicular gypsum of 85–260μm. Yellow layer in the middle is thicker, ranging from 260 to 340μm, which consists of dense platelike and framboidal gypsum crystals, smaller than 20μm. The outermost layer (left part) is black and very thin, around 30μm, constituted of acicular gypsum in 72–192μm length. Component of elements on different crystals is similar, driven by approximate forming process probably.

ZH-1b doesn't show regular gypsum crystals but porous structure (Figure 3c), while calcium sulphate can still be estimated by EDS. In contrast, rhombic gypsum in 11–28μm length and spherical particles are identified on ZH-2b (Figure 3d). $CaSO_4$(D1), SiO_2 and $CaMg(CO_3)_2$ (D2), carbonaceous fragment (D3) are evaluated. Darker acicular gypsum crystals in 33–92μm length and irregular particles are observed on ZH-3b (Figure 3e), with similar component.

Thickness of WZ-1b crust varies from 65 to 138 microns, which shows some holes and fissures on the surface (Figure 3f). Sulfur content is unusually lower than other samples, but carbon content is relatively high.

3.3. Inorganic composition

Two typical kinds of body rocks according to XRF results were studied by XRD, presented in Figure 4. Mineralogical phases of WM(SC-1a) are mainly calcium carbonate and handful muscovite, and the QM(ZH-3a) is composed of dolomite and a few quartzes.

As revealed by representative Raman spectra of the samples in Figure 5, gypsum and amorphous carbon can be identified on every black crust surface, mainly according to the strongest symmetric stretching mode of SO_4 (around 1008cm^{-1}) (Berenblut et al., 1971) in $CaSO_4{\cdot}2H_2O$ and the graphitic (around 1320cm^{-1}) and disordered (around 1580cm^{-1}) broad bands of carbon (Ferrari and Robertson, 2000), even the three layers in SC-2b. Furthermore, distinct fluorescence background or laser-induced fluorescence can be found due to organic matter, such as the soil organic matter (Milori et al., 2006), polycyclic aromatic hydrocarbons (PAHs) (Baumann et al., 2000), OH and hydrocarbon fuel fragments (Allen et al., 1995) in the crusts.

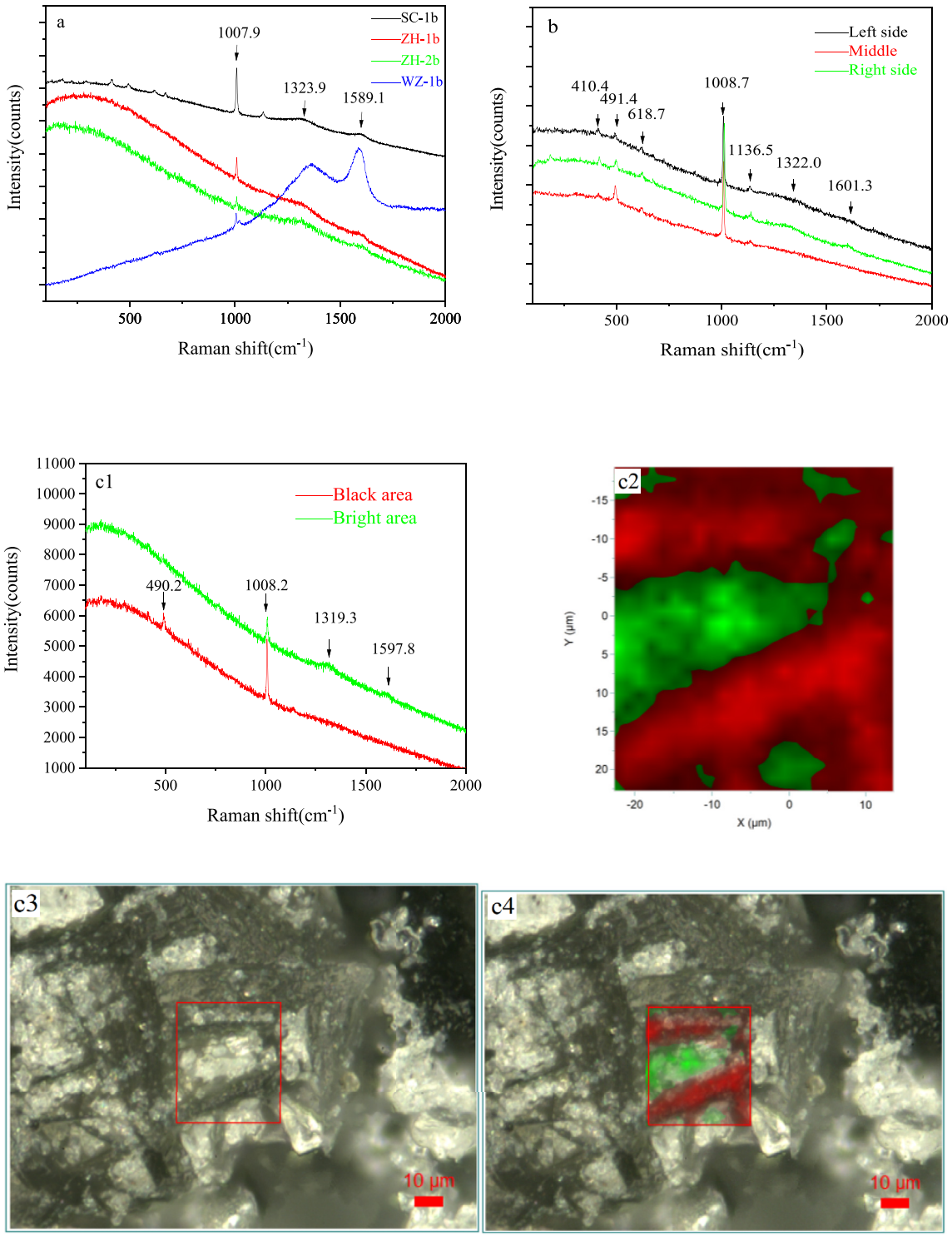

Figure 5. Raman spectra and Raman mapping results of black crusts. a: SC-1b, ZH-1b, ZH-2b, WZ-1b; b: SC-2b; c1: two kinds of components found on ZH-3b (Green-gypsum and carbon, Red-gypsum); c2: Raman image after CLS calibration; c3: mapping area on ZH-3b; c4: overlay the Raman image on micrograph of ZH-3b.

Raman mapping was taken to characterize gypsum crystals and carbon on ZH-3b, which reveals an interesting result. Raman peaks of amorphous carbon are not found in the black area, where mainly contains gypsum crystals. Whereas obvious carbon bands are observed in the bright parts. It is likely that the acicular crystals just absorb organic carbon, matching with SEM-EDS results.

3.4. Pollutant elements analysis

As the SC-1 and ZH-3 are always been in the same place since the temples were built, and WZ-1 is the only one sample we found in Museum of Western Zhou Yandu Relics storehouse, so they were analyzed in detail for more metal pollution information. Other samples can be got are not

Table 3. Results of chemical analysis of typical host rocks and black crusts by ICP-OES Unit: mg/kg.

Sample No.	Cr	Ba	Ni	Sr	Cu	Pb	Ti	Mn	Sn	Fe	K	Al	P	Zn	As
SC-1a	82.4	86.2	171.7	188.5	253.5	263.0	356.9	439.2	3051.1	4843.4	4850.4	7563.4	8820.5	<30.0	<30.0
SC-1b	176.9	163.5	2070.6	366.3	246.7	851.1	691.8	238.3	6000.2	5916.4	7233.3	11223.4	15773.5	48.53003	45.98759
ZH-3a	71.0	<30.0	1161.8	<30.0	<30.0	<30.0	<30.0	66.7	3943.4	1115.7	136.5	636.2	10038.6	<30.0	<30.0
ZH-3b	840.5	416.3	3220.3	413.5	890.3	147.2	1891.6	224.5	9452.1	13893.3	8723.3	18670.5	23509.8	162.8654	158.4059
WZ-1a	54.7	<30.0	59.8	<30.0	<30.0	<30.0	80.5	<30.0	960.4	563.0	146.4	172.9	2303.6	<30.0	<30.0
WZ-1b	<30.0	98.1	<30.0	360.7	<30.0	<30.0	155.1	47.7	<30.0	2628.3	1667.9	4007.9	335.8	30.0	<30.0

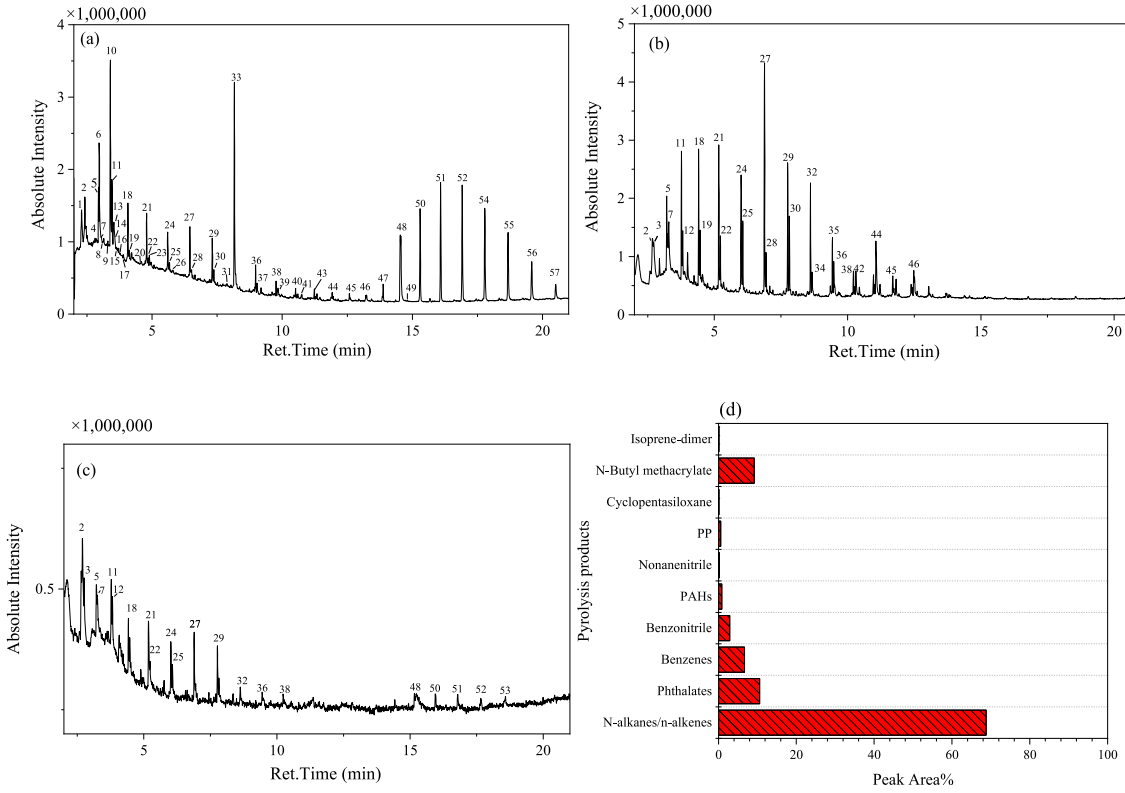

Figure 6. The total ion chromatograms of black crusts samples (a: SC-1b; b: ZH-3b; c: WZ-1b) and content of different pyrolysis products groups from SC-1b (d).

enough for ICP-OES. As shown in Table 3, the main elements content of SC-1b is higher than SC-1a, especially Cr, Ni, Sr, Pb, Sn, K, Al, P. Every pollutant element in ZH-3b is distinctly more than that in body rock, while the Ba, Sr, Ti, Mn, Fe, K and Al in WZ-1b is particularly high.

3.5. Organic compounds

The total ion chromatograms of black crusts samples are shown in Fig.6a-6c. Pyrolysis products can be classified into different groups: PAHs, n-alkanes, n-alkenes, benzenes, phthalates, isoprene dimer, presented in Table 4. Major pyrolysis organic matters in ZH-3b and WZ-1b are n-alkanes and n-alkenes (C_8–C_{29}), while products from SC-1b are more complicated since the Vajrasana Pagoda is standing at the same place for over 500 years, illustrated in Figure 6d. N-alkanes and n-alkenes, PAHs, benzenes and benzonitrile account for over 80%, phthalates take 10 percent. Besides, 9.6% is composed of n-Butyl methacrylate, cyclopentasiloxane and PP. Isoprene-dimer is also existed although very little.

4. Discussion

4.1. Pollutant sources discussion

Elements and pyrolysis products are the important indicators of the sources of pollutant in black crusts. Figure 7 shows the elements content ratio, whose values are got by ICP-OES data of black crusts divide data of host rocks, while the values below 30 are defined 30. Table 5 illustrates the sources of pollutant elements in Beijing area employed with positive matrix factorization receptor model (PMF), Enrichment factor (EF) or principal component analysis (PCA), which is helpful for evaluating the main affecting factors in the formation process. From the perspective of the elements results, vehicle exhausts, coal combustion and crust related are the main sources for pollutants on black crusts in SC, due mainly to high Ni, Pb, Cr, Sn, Ti, Ba, Zn, As, Al level. For ZH, extremely abundant K, Ti, Cu, Al, Ba, Fe, Cr and relatively high Zn, As, Pb indicate coal combustion, biomass burning, vehicle exhausts and crust related are key factors. Meanwhile, another important factor should be considered from increasing contents of Sr, K, P and Mn. SC and ZH were famous temples before they became museums. So, incense burning, as a religious ceremony, which had lasted for over 500 years, as well as biomass burning from monks, contributed to the formation of BCs before the industrial age. For WZ-1b, crust related and biomass burning perhaps have more effects on the formation process, based primarily on more Al, Sr, K, Fe, Ba, Ti and Mn. Additionally, high Si contents of SC-5b and ZH-2b through pXRF perhaps come from residue of organosilyl conservation materials used before, according to the administrator's memory.

About the organic compounds, there are some studies on the deposits through Pyrolysis-GC/MS can be valuable references, as listed in Table 6.

Table 4. Pyrolysis products identified by py-GCMS (× = Not identified, √ = Identified).

Peaks	Identified compounds	SC-1b	ZH-3b	WZ-1b	Peaks	Identified compounds	SC-1b	ZH-3b	WZ-1b
1	Bicyclo [5.1.0]octane				30	Pentadecane		√	
2	1-Octene		√	√	31	Nonyl benzene			
3	Octane	×	√	√	32	1-Hexadecene	×	√	√
4	o-Xylene				33	Diethyl phthalate			
5	1-Nonene		√	√	34	Hexadecane	×	√	
6	Styrene				35	Heptadecane	×	√	
7	Nonane		√	√	36	1-Heptadecene		√	√
8	Cyclotetrasiloxane, octamethyl-				37	3-Nonen-1-ol, (E)-			
9	Benzene, propyl-				38	1-Octadecene		√	√
10	n-Butyl methacrylate				39	Phenanthrene			
11	1-Decene		√	√	40	PP			
12	Decane	×	√	√	41	Nonanenitrile			
13	Benzonitrile				42	1-Nonadecene	×	√	
14	Benzofuran				43	Dibutyl phthalate			
15	Phenol				44	1-Eicosene		√	
16	isoprene-dimer				45	1-Heneicosene		√	
17	Benzene, butyl-				46	1-Docosene		√	
18	1-Undecene		√	√	47	Tetracosane			
19	Undecane		√		48	Pentacosane			√
20	Benzene, pentyl-				49	Diisooctyl phthalate			
21	1-Dodecene		√	√	50	Hexacosane			√
22	Dodecane		√	√	51	Heptacosane			√
23	Naphthalene				52	Octacosane			√
24	1-Tridecene		√	√	53	Nonacosane	×		√
25	Tridecane		√	√	54	Triacontane			
26	Naphthalene, 2-methyl-				55	Hentriacontane			
27	1-Tetradecene		√	√	56	Dotriacontane			
28	Tetradecane		√		57	Tetratriacontane			
29	1-Pentadecene		√	√					

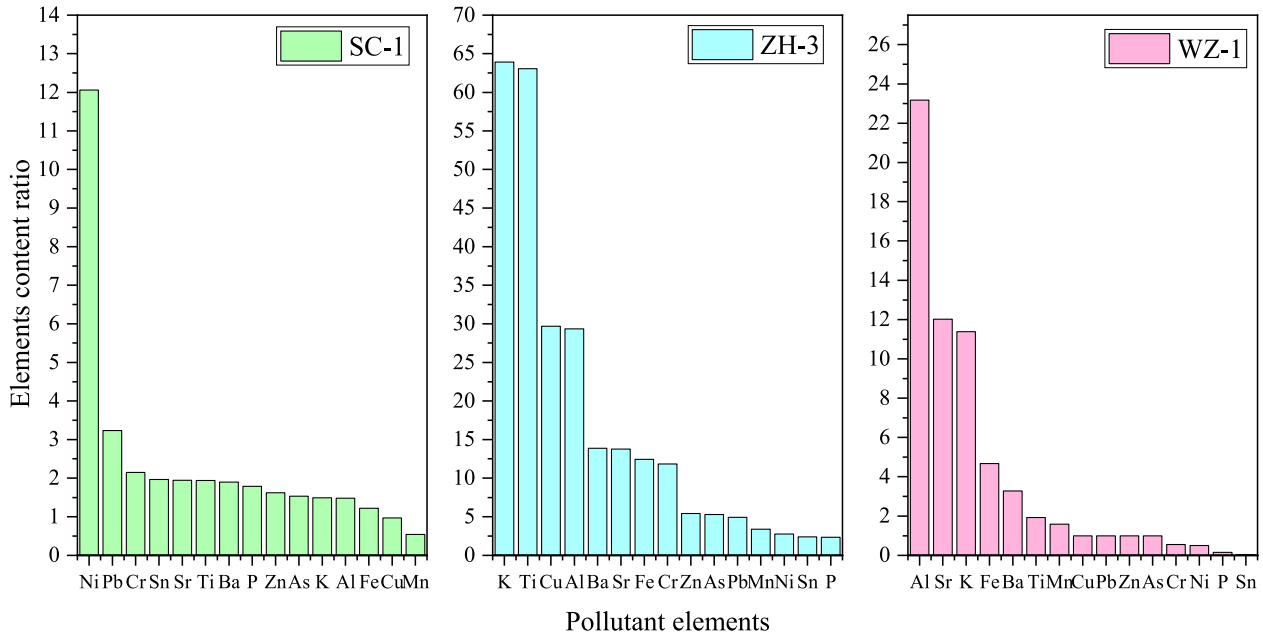

Figure 7. Content ratio between elements in black crusts and host rocks.

Major pyrolysis organic matters in ZH-3b and WZ-1b are n-alkanes and n-alkenes, probably attributed to biomass and fossil fuel combustions. Products from SC-1b are more complicated shown in Figure 6. N-alkanes and n-alkenes, PAHs, benzenes and benzonitrile are the main compounds, which have similar sources from black carbon as a product of incomplete combustion of biomass, fossil fuels, and coal. Phthalates, mostly coming from plastic products, take 10 percent. In addition, there is a good possibility that n-Butyl methacrylate, cyclopentasiloxane and

Table 5. Major sources of pollutant elements in Beijing area.

Elements in the crusts	Major sources in Beijing area
Cr	Coal combustion (46.6%), Oil combustion (30.5%), Iron and steel industry (14.3%) (Cheng et al., 2014); vehicle exhausts (Duan et al., 2010); Waste Incineration (Astrup et al., 2005)
Ba, Ti, Al	Crust related, vehicle exhausts (Duan et al., 2012; Yu et al., 2013)
Ni	Vehicle exhausts, suspended soil, coal combustion (Kuang et al., 2004; Duan et al., 2012)
Sr	Incense Burning (Chen et al., 2021a,b), coal combustion (Duan et al., 2012)
Cu	Vehicle exhausts, Industrial combustion (Kuang et al., 2004; Duan et al., 2012)
Pb	Before 1997–1998, vehicle exhausts; after 1997–1998, emissions from metal, lead-related, refining plants, coal combustion (Duan et al., 2006, 2012)
Mn	Vehicle exhausts, Iron and steel production, Incense Burning (Kuang et al., 2004; Duan et al., 2012; Yu et al., 2013; Chen et al., 2021a,b)
Sn	Crust soil/re-suspended soil, Vehicle exhausts, Coal combustion (Duan et al., 2012)
Fe	Crust related, Iron and steel production, Vehicle exhausts (Kuang et al., 2004; Duan et al., 2012; Yu et al., 2013)
K	Coal combustion, biomass burning (Yu et al., 2013, 2018; Chen et al., 2017)
P	Straw burning (Meng et al., 2022)
Zn	Vehicle exhaust, Brakers (Kuang et al., 2004; Yu et al., 2013)
As	Coal combustion (Duan et al., 2012)

Table 6. Major sources of pyrolysis products from deposits.

Component classes	Major sources
PAHs:	Black carbon in soil, charcoal, fossil fuel combustion, biomass/coal burning (Kaal et al., 2008, 2009; Sykorova et al., 2011; Chen et al., 2017; Fang et al., 2021)
Benzene series	Black carbon in soil/EC (Kaal et al., 2008, 2009)
Benzonitrile	Black carbon (a product of incomplete combustion of vegetation, fossil fuels, and coal soot) (Kaal et al., 2008; Sý korov á et al., 2009)
Phthalates	plastic products (Zhang et al., 2014; Li et al., 2016)
N-alkanes/n-alkenes	Biomass combustions and Fossil fuel combustion in heating seasons, plant waxes in other seasons (Kaal et al., 2009; Duan et al., 2010; Kang et al., 2018)
Isoprene-dimer	Tire tread particles (Unice et al., 2012)

PP are derived from conservation materials used, such as silicone (Favaro et al., 2007) and acrylic resins (Melo et al., 1999). A tiny part of isoprene-dimer is likely a consequence of tire tread.

In summary, pollutants on SC-1b are coming from vehicle exhausts, coal combustion, biomass and incense burning, plastic products and soils. Part of the Vajrasana Pagoda was treated by silicone or acrylic resins before, but the materials have been invalidated for a long time, subsequently forming the black crusts. The ZH-3b are affected by vehicle exhausts, coal combustion, biomass, crust related and incense burning, industrial emission. As for WZ-1b, biomass burning and crust soil are the major causes of black part, matching with its blackened morphology.

4.2. Black crust forming mechanism discussion

Typically, calcium sulfate precipitation and carbonaceous particles are two important factors in the process of black crusts forming. According to the morphological results, there are a large number of idiomorphic gypsum crystals on the crusts, with bigger size than PM_{10} and $PM_{2.5}$. Therefore, it is probable that the gypsum is not from the deposition of atmospheric sulphate but rather from reaction between the carbonate and sulfur compounds, which is consistent with isotopic data (Genot et al., 2020; Aroskay et al., 2021).

The climate and air quality of Beijing (Figure 8) should be considered during the process of black crusts forming. O_3 concentration, illustrated in Figure 8a, is obviously high in summer, as a consequence of emissions of NO_x and VOCs from vehicle exhaust and industry in Beijing (He et al., 2022). Sulfuric acid is formed from oxidation by O_3, H_2O_2, OH radicals (Berglen et al., 2004), since strong solar radiation at low relative humidity (RH) and the high temperature are beneficial to the formation of acid rain precursors (Hamed et al., 2011), leading to a low median pH of acid rain in Beijing from June to September (Sun et al., 2021). As a result, frequent sulphation process occurs on the marble surface in this period, demonstrated in Figure 9. SiO_2 oxidation by O_2 with metal ion catalysts also contributes to the sulphation (Aroskay et al., 2021), since Al, Mn, Fe, Ni, Cu, Zn, et al. can be detected in the rainwater (Vlastos et al., 2019) and crusts.

In nature the calcium sulfate is found in three phases distinguished by the degree of hydration: gypsum ($CaSO_4{\cdot}2H_2O$), bassanite or hemihydrate ($CaSO_4{\cdot}0.5H_2O$) and anhydrite ($CaSO_4$ or γ-CaSO4) (Cunningham et al., 1952; Freyer and Voigt, 2003). After $CaCO_3$ or $CaMg(CO_3)_2$ reacting with sulfide, bassanite will become the stable precursor phase to gypsum precipitation firstly (Wang et al., 2012; Van Driessche et al., 2012; Stawski et al., 2016), when the concentration increasing due to water evaporating in the water-remaining area on sculptures. Then homogeneous nucleation occurs from the bulk of solution, or heterogeneous nucleation occurs on the surface of existing crystals according to the classical nucleation theory (Reznik et al., 2012; Rendel et al., 2018; Reiss et al., 2019). The morphology depends on the saturation state of a solution with regard to gypsum (Ω_{gypsum}) and the mixtures in the solution. Stellate crystals are formed by homogeneous nucleation when $\Omega_{gypsum} > 4.4$, far from equilibrium oversaturation, while plate-like and acicular crystals are formed by heterogeneous nucleation when $\Omega_{gypsum} < 2.15$, close to equilibrium (Reiss et al., 2019). As can be seen in the microscopy results, gypsum crystals are mainly consequence of heterogeneous nucleation.

On $CaCO_3$ (White calcitic marble) surface, the reaction products with sulfide are calcium sulfate simply. Nevertheless, Mg^{2+} will participate in

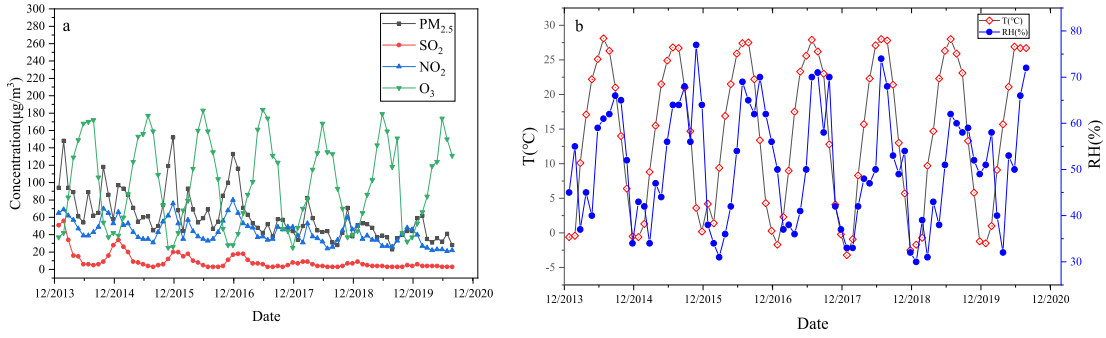

Figure 8. Air quality(a), ambient temperature and relative humidity(b) from January 2014 to August 2020 in Beijng

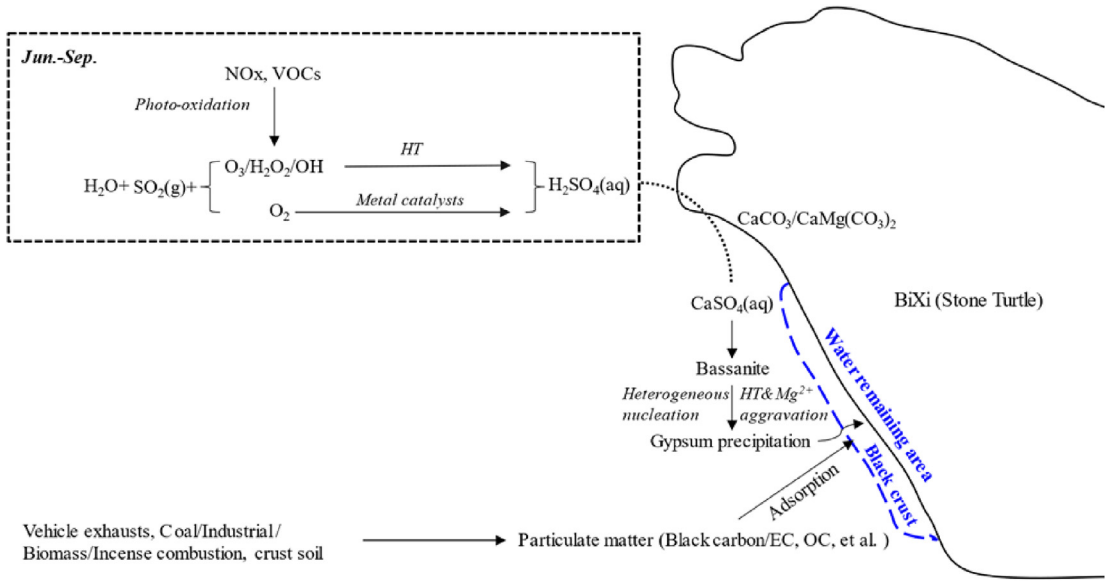

Figure 9. Forming process of black crust on marble sculptures in Beijing, taking BiXi as an example (HT = high temperature).

the nucleation process on $CaMg(CO_3)_2$ (QM) surface. The solubility of gypsum decreases with the existence of bivalent metal sulfate, especially the $MgSO_4$(Cameron and Bell, 1906; Wollmann and Voigt, 2008). This is probably why many large crusts were found on QM sculptures, although the open porosity and free water absorption are just 0.853% and 0.197% (Liu et al., 2019).

$$\Omega\text{gypsum} = \frac{\text{IAP}}{K_{sp}} = \frac{a_{Ca^{2+}} \cdot a_{SO_4^{2-}} \cdot a_{H_2O}^2}{\left(a_{Ca^{2+}} \cdot a_{SO_4^{2-}} \cdot a_{H_2O}^2\right)_{eq}} \quad (1)$$

Eq. (1). Where IAP is the ion activity product, K_{sp} is the solubility constant, and a_i is the activity of the i^{th} constituent (Reiss et al., 2019).

Additionally, the maximum solubility of gypsum is given at 40 °C, from where the value decreases with the temperature, discovered by George A. Hulett and Lucius E (George and Lucius, 1902). Thus, the high ambient temperature and more precipitation in summer (Figure 8b) contribute to thicker gypsum deposit. Carbonaceous particles, mainly related to organic carbon (OC) and elemental carbon (EC) from $PM_{2.5}$ (He et al., 2001), have higher concentration in fall and winter, as shown in Figure 8a. Although the photochemistry is weak in winter, sulfate can be formed from SO_2 oxidized by NO_2 in aerosol, who would be a major component of haze particles (Cheng et al., 2016). Suspended particles are captured by porous gypsum, then soluble salts will be washed away and the undissolved matters (e.g., EC/black carbon) stay on the crusts, leading to the black crusts. In addition, organic carbon is more likely intrude into gypsum crystals, which is like that Ca^{2+} can creating cationic bridges between organic matter and clay particles to increase the soil organic carbon (Tisdall and Oades, 1982; Inagaki et al., 2016, 2017).

5. Conclusions

In this work, black crusts and body rocks from three important cultural heritage sites in Beijing were analyzed by several analytical methods. Two kinds of marble are found and the major one is QM, composed of dolomite and a few quartzes, while the other one is WM, consisted of calcium carbonate and handful muscovite. The black crusts mainly contain gypsum and disordered carbon. Pollutant elements analysis data (higher metal and P, as contents in black crusts) and pyrolysis products (N-alkanes/n-alkenes, PAHs, benzonitrile, benzene series and phthalates) give an indicator of the pollution sources. Vehicle exhausts, coal combustion, biomass burning and crust related are the main sources of pollutants on black crusts in high urbanization sites. Besides, incense burning should be considered as one of the sources in temple sites before industrial age. The samples from WZ, which is far away from center of city, biomass burning and crust soil is the major cause of black crusts.

Combining morphology results and atmospheric data, the formation of black crusts in Beijing can be deduced. In summer and fall, acid rain occurs with high probability due to high O_3 level, high temperature and humidity. After the carbonate and sulfur compounds reacting, heterogeneous nucleation proceeds to form rhombic, plate-like and acicular gypsum crystals. Driven by a special solubility, more gypsum precipitates at high ambient temperature. Furthermore, existence of Mg^{2+} and other bivalent metal sulfate will decrease the solubility of gypsum greatly, resulting in easier precipitation on $CaMg(CO_3)_2$ (QM) surface. These idiomorphic gypsum crystals form a mesh that capture suspended particulates passively, especially in winter, when the concentration of $PM_{2.5}$ is high. The undissolved particles (EC, OC and Soil) will be embedded in the net and become part of crusts. Sulfate or $CaSO_4$ derived from aerosol is not the main source of gypsum on black crusts, demonstrated by SEM-EDS. Intriguingly, it is probable that the acicular crystals have strong absorption of organic carbon and needs further investigation to figure out the mechanism.

Declarations

Author contribution statement

Feng Wang: Conceived and designed the experiments; Performed the experiments; Analyzed and interpreted the data; Wrote the paper.

Yingchun Fu & Yazhen Huang: Performed the experiments; Analyzed and interpreted the data.

Di Li: Contributed reagents, materials, analysis tools or data.

Shuya Wei: Analyzed and interpreted the data; Wrote the paper.

Funding statement

Shuya Wei was supported by Beijing Municipal Cultural Heritage Bureau [11000022T000000477642].

Data availability statement

Data included in article/supp. material/referenced in article.

Declaration of interests statement

The authors declare no conflict of interest.

Additional information

Supplementary content related to this article has been published online at https://doi.org/10.1016/j.heliyon.2022.e10442.

Acknowledgements

Thank ZHIHUA Temple and Museum of Western Zhou Yandu Relics for the help during the investigation.

References

Allen, M.G., McManus, K.R., Sonnenfroh, D.M., Paul, P.H., 1995. Planar laser-induced-fluorescence imaging measurements of OH and hydrocarbon fuel fragments in high-pressure spray-flame combustion. Appl. Opt. 34, 6287–6300.

Aroskay, A., Martin, E., Bekki, S., Montana, G., Randazzo, L., Cartigny, P., et al., 2021. Multi O- and S-isotopes as tracers of black crusts formation under volcanic and non-volcanic atmospheric conditions in Sicily (Italy). Sci. Total Environ. 750, 142283.

Astrup, T., Rosenblad, C., Trapp, S., Christensen, T.H., 2005. Chromium release from waste incineration air-pollution-control residues. Environ. Sci. Technol. 39 (9), 3321–3329.

B Belfiore, C.M., Barca, D., Bonazza, A., Comite, V., La Russa, M.F., Pezzino, A., et al., 2013. Application of spectrometric analysis to the identification of pollution sources causing cultural heritage damage. Environ. Sci. Pollut. Res. 20, 8848–8859.

Bao, L., Ma, K., Xu, X., et al., 2019. Foliar particulate matter distribution in urban road system of beijing, China. Chin. Geogr. Sci. 29, 591–600.

Barca, D., Comite, V., Belfiore, C.M., Bonazza, A., La Russa, M.F., Ruffolo, S.A., et al., 2014. Impact of air pollution in deterioration of carbonate building materials in Italian urban environments. Appl. Geochem. 48, 122–131.

Baumann, T., Haaszio, S., Niessner, R., 2000. Applications of a laser-induced fluorescence spectroscopy sensor in aquatic systems. Water Res. 34 (4), 1318–1326.

Berenblut, B.J., Dawson, P., Wilkinson, G.R., 1971. The Raman spectrum of gypsum. Acta A Mol. Biomol. Spectrosc. 27 (9), 1849–1863.

Berglen, T.F., Berntsen, T.K., Isaksen, I.S.A., Sundet, J.K., 2004. A global model of the coupled sulfur/oxidant chemistry in the troposphere: the sulfur cycle. J. Geophys. Res. 109.

Bonazza, A., Sabbioni, C., Ghedini, N., 2005. Quantitative data on carbon fractions in interpretation of black crusts and soiling on European built heritage. Atmos. Environ. 39, 2607–2618.

Bugini, R., Tabasso, M.L., Realini, M., 2000. Rate of formation of black crusts on marble. A case study. J. Cult. Herit. 1, 111–116.

Cameron, F.K., Bell, J.M., 1906. The solubility of gypsum in magnesium sulphate solutions. J. Phys. Chem. 10, 210–215.

Camuffo, D., Del Monte, M., Sabbioni, C., 1983. Origin and growth mechanisms of the sulfated crusts on urban limestone. Water Air Soil Pollut. 19, 351–359.

Chen, J., Li, C., Ristovski, Z., Milic, A., Gu, Y., Islam, M.S., et al., 2017. A review of biomass burning: emissions and impacts on air quality, health and climate in China. Sci. Total Environ. 579, 1000–1034.

Chen, G., Hu, Y., Zhang, R., Yin, Z., Zhang, Y., Ma, K., 2021a. Evolution of south-north transport and urbanization effects on PM2.5 distribution with increased pollution levels in Beijing. Sustain. Cities Soc. 72.

Chen, K.F., Tsai, Y.P., Lai, C.H., Xiang, Y.K., Chuang, K.Y., Zhu, Z.H., 2021b. Human health-risk assessment based on chronic exposure to the carbonyl compounds and metals emitted by burning incense at temples. Environ. Sci. Pollut. Res. Int. 28, 40640–40652.

Cheng, H., Zhou, T., Li, Q., Lu, L., Lin, C., 2014. Anthropogenic chromium emissions in China from 1990 to 2009. PLoS One 9 (2), e87753.

Cheng, Yafang, Zheng, Guangjie, Wei, Chao, Mu, Qing, Zheng, Bo, Wang, Zhibin, et al., 2016. Reactive nitrogen chemistry in aerosol water as a source of sulfate during haze events in China. Sci. Adv. 2, e1601530.

Comite, V., Pozo-Antonio, J.S., Cardell, C., Randazzo, L., La Russa, M.F., Fermo, P., 2020. A multi-analytical approach for the characterization of black crusts on the facade of an historical cathedral. Microchem. J. 158.

Cunningham, W.A., Dunham, R.M., Antes, L.L., 1952. Hydration of gypsum plaster. Ind. Eng. Chem. 44 (10), 2402–2408.

Duan, F.K., He, K.B., Ma, Y.L., Yang, F.M., Yu, X.C., Cadle, S.H., et al., 2006. Concentration and chemical characteristics of PM2.5 in Beijing, China: 2001-2002. Sci. Total Environ. 355, 264–275.

Duan, F., He, K., Liu, X., 2010. Characteristics and source identification of fine particulate n-alkanes in Beijing, China. J. Environ. Sci. 22, 998–1005.

Duan, J., Tan, J., Wang, S., Hao, J., Chai, F., 2012. Size distributions and sources of elements in particulate matter at curbside, urban and rural sites in Beijing. J. Environ. Sci. 24, 87–94.

Fang, H., Luo, S., Huang, X., Fu, X., Xiao, S., Zeng, J., et al., 2021. Ambient Naphthalene and Methylnaphthalenes Observed at an Urban Site in the Pearl River Delta Region: Sources and Contributions to Secondary Organic Aerosol, 252. Atmospheric Environment.

Farkas, O., Siegesmund, S., Licha, T., Török, Á., 2018. Geochemical and mineralogical composition of black weathering crusts on limestones from seven different European countries. Environ. Earth Sci. 77.

Favaro, M., Mendichi, R., Ossola, F., Simon, S., Tomasin, P., Vigato, P.A., 2007. Evaluation of polymers for conservation treatments of outdoor exposed stone monuments. Part II: photo-oxidative and salt-induced weathering of acrylic–silicone mixtures. Polym. Degrad. Stabil. 92, 335–351.

Ferrari, A.C., Robertson, J., 2000. Interpretation of Raman spectra of disordered and amorphous carbon. Phys. Rev. B Condens. Matter 61, 14095–14105.

Freyer, D., Voigt, W., 2003. Crystallization and phase stability of CaSO4 and CaSO4 – based salts. Monatsh. Chem. 134, 693–719.

Fronteau, G., Schneider-Thomachot, C., Chopin, E., Barbin, V., Mouze, D., Pascal, A., 2010. Black-crust growth and interaction with underlying limestone microfacies. Geol. Soc. London, Special Publications 333, 25–34.

Galletti, G.C., Bocchini, P., Cam, D., Chiavari, G., Mazzeo, R., 1997. Chemical characterization of the black crust present on the stone central portal of St. Denis abbey. Fresenius' J. Anal. Chem. 357, 1211–1214.

García-Florentino, C., Maguregui, M., Ciantelli, C., Sardella, A., Bonazza, A., Queralt, I., et al., 2020. Deciphering past and present atmospheric metal pollution of urban environments: the role of black crusts formed on historical constructions. J. Clean. Prod. 243.

Genot, I., Au Yang, D., Martin, E., Cartigny, P., Legendre, E., De Rafelis, M., 2020. Oxygen and sulfur mass-independent isotopic signatures in black crusts: the complementary negative Δ33S reservoir of sulfate aerosols? Atmos. Chem. Phys. 20, 4255–4273.

George, A.H., Lucius, E.A., 1902. The solubility of gypsum. J. Am. Chem. Soc. 24 (7), 667–679.

Hamed, A., Korhonen, H., Sihto, S.-L., Joutsensaari, J., Järvinen, H., Petäjä, T., et al., 2011. The role of relative humidity in continental new particle formation. J. Geophys. Res. 116.

He, Kebin, Yang, Fumo, Ma, Yongliang, Zhang, Qiang, Yao, Xiaohong, Chan, Chak K., Cadle, Steven, Chan, Tai, Mulawa, Patricia, 2001. The characteristics of PM2.5 in Beijing, China. Atmos. Environ. 35 (29), 4959–4970.

He, Z., Liu, P., Zhao, X., He, X., Liu, J., Mu, Y., 2022. Responses of surface O3 and PM2.5 trends to changes of anthropogenic emissions in summer over Beijing during 2014-2019: a study based on multiple linear regression and WRF-Chem. Sci. Total Environ. 807, 150792.

Inagaki, T.M., de Moraes Sá, J.C., Caires, E.F., Gonçalves, D.R.P., 2016. Lime and gypsum application increases biological activity, carbon pools, and agronomic productivity in highly weathered soil. Agric. Ecosyst. Environ. 231, 156–165.

Inagaki, T.M., de Moraes Sa, J.C., Caires, E.F., Goncalves, D.R.P., 2017. Why does carbon increase in highly weathered soil under no-till upon lime and gypsum use? Sci. Total Environ. 599–600, 523–532.

Kaal, J., Martínez-Cortizas, A., Nierop, K.G.J., Buurman, P., 2008. A detailed pyrolysis-GC/MS analysis of a black carbon-rich acidic colluvial soil (Atlantic ranker) from NW Spain. Appl. Geochem. 23, 2395–2405.

Kaal, J., Martínez Cortizas, A., Nierop, K.G.J., 2009. Characterisation of aged charcoal using a coil probe pyrolysis-GC/MS method optimised for black carbon. J. Anal. Appl. Pyrolysis 85, 408–416.

Kang, M., Ren, L., Ren, H., Zhao, Y., Kawamura, K., Zhang, H., et al., 2018. Primary biogenic and anthropogenic sources of organic aerosols in Beijing, China: insights from saccharides and n-alkanes. Environ. Pollut. 243, 1579–1587.

Kuang, C., Neumann, T., Norra, S., et al., 2004. Land use-related chemical composition of street sediments in beijing. Environ. Sci. Pollut. Res. 11, 73.

La Russa, M.F., Fermo, P., Comite, V., Belfiore, C.M., Barca, D., Cerioni, A., et al., 2017. The Oceanus statue of the Fontana di Trevi (Rome): the analysis of black crust as a tool to investigate the urban air pollution and its impact on the stone degradation. Sci. Total Environ. 593–594, 297–309.

Lamhasni, T., El-Marjaoui, H., El Bakkali, A., Lyazidi, S.A., Haddad, M., Ben-Ncer, A., et al., 2019. Air pollution impact on architectural heritage of Morocco: combination of synchronous fluorescence and ATR-FTIR spectroscopies for the analyses of black crusts deposits. Chemosphere 225, 517–523.

Li, C., Chen, J., Wang, J., Han, P., Luan, Y., Ma, X., et al., 2016. Phthalate esters in soil, plastic film, and vegetable from greenhouse vegetable production bases in Beijing, China: concentrations, sources, and risk assessment. Sci. Total Environ. 568, 1037–1043.

Liu, J-b, Zhang, Z-j, Li, B., 2019. Microscopic & macroscopic characterizations of Beijing marble as a building material for UNESCO heritage sites: new insights into physico-mechanical property estimation and weathering resistance. Construct. Build. Mater. 225, 510–525.

Marinoni, N., Birelli, M.P., Rostagno, C., Pavese, A., 2003. The effects of atmospheric multipollutants on modern concrete. Atmos. Environ. 37, 4701–4712.

Melo, M.J., Bracci, S., Camaiti, M., Chiantore, O., Piacenti, F., 1999. Photodegradation of acrylic resins used in the conservation of stone. Polym. Degrad. Stabil. 66 (1), 23–30.

Meng, Y., Li, R., Cui, L., Wang, Z., Fu, H., 2022. Phosphorus emission from open burning of major crop residues in China. Chemosphere 288, 132568.

Milori, D.M.B.P., Galeti, H.V.A., Martin-Neto, L., Dieckow, J., González-Pérez, M., Bayer, C., et al., 2006. Organic matter study of whole soil samples using laser-induced fluorescence spectroscopy. Soil Sci. Soc. Am. J. 70, 57–63.

Nadia, G., Cristina, S., Alessandra, B., Giancarlo, G., 2006. Chemical-thermal quantitative methodology for carbon speciation in damage layers on building surfaces. Environ. Sci. Technol. 40, 939–944.

Nord, A.G., Ericsson, T., 1993. Chemical analysis of thin black layers on building stone. Stud. Conserv. 38, 25–35.

Pak, U., Ma, J., Ryu, U., Ryom, K., Juhyok, U., Pak, K., Pak, C., 2020. Deep learning-based PM2.5 prediction considering the spatiotemporal correlations: a case study of Beijing, China. Sci. Total Environ. 699, 133561.

Potgieter-Vermaak, S.S., Godoi, R.H., Grieken, R.V., Potgieter, J.H., Oujja, M., Castillejo, M., 2005. Micro-structural characterization of black crust and laser cleaning of building stones by micro-Raman and SEM techniques. Spectrochim. Acta Mol. Biomol. Spectrosc. 61, 2460–2467.

Pozo-Antonio, J.S., Pereira, M.F.C., Rocha, C.S.A., 2017. Microscopic characterisation of black crusts on different substrates. Sci. Total Environ. 584–585, 291–306.

Reiss, A.G., Ganor, J., Gavrieli, I., 2019. Size distribution and morphology of gypsum crystals precipitating from hypersaline solutions. Cryst. Growth Des. 19, 6954–6962.

Rendel, P.M., Gavrieli, I., Wolff-Boenisch, D., Ganor, J., 2018. Towards establishing a combined rate law of nucleation and crystal growth – the case study of gypsum precipitation. J. Cryst. Growth 485, 28–40.

Reznik, I.J., Ganor, J., Gruber, C., Gavrieli, I., 2012. Towards the establishment of a general rate law for gypsum nucleation. Geochem. Cosmochim. Acta 85, 75–87.

Rivas, T., Pozo, S., Paz, M., 2014. Sulphur and oxygen isotope analysis to identify sources of sulphur in gypsum-rich black crusts developed on granites. Sci. Total Environ. 482–483, 137–147.

Ruffolo, S.A., Comite, V., La Russa, M.F., Belfiore, C.M., Barca, D., Bonazza, A., et al., 2015. An analysis of the black crusts from the Seville Cathedral: a challenge to deepen the understanding of the relationships among microstructure, microchemical features and pollution sources. Sci. Total Environ. 502, 157–166.

Russa, M.F., Belfiore, C.M., Comite, V., Barca, D., Bonazza, A., Ruffolo, S.A., et al., 2013. Geochemical study of black crusts as a diagnostic tool in cultural heritage. Appl. Phys. A 113, 1151–1162.

Sabbioni, C., 1995. Contribution of atmospheric deposition to the formation of damage layers. Sci. Total Environ. 167, 49–55.

Samara, C., Melfos, V., Kouras, A., Karali, E., Zacharopoulou, G., Kyranoudi, M., et al., 2020. Morphological and geochemical characterization of the particulate deposits and the black crust from the Triumphal Arch of Galerius in Thessaloniki, Greece: implications for deterioration assessment. Sci. Total Environ. 734, 139455.

Stawski, T.M., van Driessche, A.E.S., Ossorio, M., Diego Rodriguez-Blanco, J., Besselink, R., Benning, L.G., 2016. Formation of calcium sulfate through the aggregation of sub-3 nanometre primary species. Nat. Commun. 7, 11177.

Sun, S., Liu, S., Li, L., Zhao, W., 2021. Components, acidification characteristics, and sources of atmospheric precipitation in Beijing from 1997 to 2020. Atmos. Environ. 266.

Sýkorová, I., Havelcová, M., Trejtnarová, H., Matysová, P., Vašíček, M., Kříbek, B., et al., 2009. Characterization of organic matter in dusts and fluvial sediments from exposed areas of downtown Prague, Czech Republic. Int. J. Coal Geol. 80, 69–86.

Sykorova, I., Havelcova, M., Zeman, A., Trejtnarova, H., 2011. Carbon air pollution reflected in deposits on chosen building materials of Prague Castle. Sci. Total Environ. 409, 4606–4611.

Tisdall, J., Oades, J.M., 1982. Organic matter and water-stable aggregates in soils. J. Soil Sci. 33, 141–163.

(Yuan Dynasty) Tuotuo, 1995. History of Jin Dynasty. Jilin People's Press, p. 459 (in chinese).

Unice, K.M., Kreider, M.L., Panko, J.M., 2012. Use of a deuterated internal standard with pyrolysis-GC/MS dimeric marker analysis to quantify tire tread particles in the environment. Int. J. Environ. Res. Publ. Health 9, 4033–4055.

Van Driessche, A.E.S., Benning, L.G., Rodriguez-Blanco, J.D., Ossorio, M., Bots, P., García-Ruiz, J.M., 2012. The role and implications of bassanite as a stable precursor phase to gypsum precipitation. Science 336, 69–72.

Vlastos, D., Antonopoulou, M., Lavranou, A., Efthimiou, I., Dailianis, S., Hela, D., et al., 2019. Assessment of the toxic potential of rainwater precipitation: first evidence from a case study in three Greek cities. Sci. Total Environ. 648, 1323–1332.

Wang, Y.W., Kim, Y.Y., Christenson, H.K., Meldrum, F.C., 2012. A new precipitation pathway for calcium sulfate dihydrate (gypsum) via amorphous and hemihydrate intermediates. Chem. Commun. 48, 504–506.

Wang, Z., Zhang, Z., Wang, F., Liu, J., 2022. A pXRF-based approach to identifying the material source of stone cultural relics: a case study. Minerals 12 (2), 199.

Wollmann, Georgia, Voigt, Wolfgang, 2008. Solubility of gypsum in MSO4 solutions (M = Mg, Mn, Co, Ni, Cu, Zn) at 298.15 K and 313.15 K. J. Chem. Eng. Data 53 (6), 1375–1380.

Ming Dynasty Xiao, Xun, 1983. Heritage Record of the Forbidden City. Beijing ancient book press, p. 73 (in chinese).

Yu, L., Wang, G., Zhang, R., Zhang, L., Song, Y., Wu, B., et al., 2013. Characterization and source apportionment of PM2.5 in an urban environment in beijing. Aerosol Air Qual. Res. 13, 574–583.

Yu, J., Yan, C., Liu, Y., Li, X., Zhou, T., Zheng, M., 2018. Potassium: a tracer for biomass burning in beijing? Aerosol Air Qual. Res. 18, 2447–2459.

Zhang, Z., He, G., Peng, X., Lu, L., 2014. Distribution and sources of phthalate esters in the topsoils of Beijing, China. Environ. Geochem. Health 36, 505–515.

Zhang, T., Li, D.Q., Zhang, Z.J., 2016. Damage categories and deterioration mechanism of stone cultural relics of white marble in Beijing. Geo. Inv&Surveying. 11, 7–13 (in chinese).